A carboxylate- and pyridine-based organic anode material for K-ion batteries

Journal:	*New Journal of Chemistry*
Manuscript ID	NJ-ART-07-2022-003447.R1
Article Type:	Paper
Date Submitted by the Author:	30-Aug-2022
Complete List of Authors:	Holguin, Kathryn; George Mason University, Chemistry and Biochemistry Qin, Kaiqiang; George Mason University, Chemistry and Biochemistry Huang, Jinghao; George Mason University, Chemistry and Biochemistry Luo, Chao; George Mason University, Chemistry and Biochemistry

SCHOLARONE™
Manuscripts

A carboxylate- and pyridine-based organic anode material for K-ion batteries

Kathryn Holguin,[a] Kaiqiang Qin,[a] Jinghao Huang,[a] Chao Luo,*[a,b]

[a]Department of Chemistry and Biochemistry, George Mason University, Fairfax, VA, 22030, USA

[b]Quantum Science & Engineering Center, George Mason University, Fairfax, VA, 22030, USA

*Corresponding author: cluo@gmu.edu

Abstract

Developing high-capacity, stable, and sustainable K-ion batteries (KIBs) is an ongoing challenge due to a lack of high-performance and environmentally benign electrode materials. To address this challenge, organic electrode materials with low cost, abundance, high sustainability, high tunability and flexibility offer opportunities. Herein, we report a novel N-containing carboxylate salt, $K_2C_{12}H_6N_2O_4$ (K-DCA) with two bipyridine moieties and two carboxylate groups. The carboxylate- and pyridine-based active centers in K-DCA can reversibly react with four K-ions to provide a specific capacity of 163.3 mAh g^{-1} with a pair of redox plateaus centered at ~0.8 V. When coupling with nitrogen-doped reduced graphene oxide (NrGO), the composite anode material, K-DCA-NrGO, demonstrates a high specific capacity of 225.25 mAh g^{-1} and increased capacity retention during long-term cycling. Additionally, reaction kinetics and mechanism studies demonstrate that the composite exhibits low overpotentials, low interphase resistance, a partial pseudo-capacitance behavior, and stable chemical/morphological structures upon cycling, which contribute to the fast kinetics and long cycle life.

1. Introduction

Li-ion batteries (LIBs) are the dominant energy storage devices in portable electronics, electric vehicles, and grid-scale stationary energy storage due to their high energy density and long cycle life. However, the large-scale applications of LIBs have triggered concerns about the scarcity, high cost, and toxicity of lithium and transition metal resources, as well as the recycling of spent LIBs. To address these challenges and satisfy the ever-growing demands for energy and environmental sustainability, K-ion batteries (KIBs) based on the abundant, low-cost, and high-sustainability potassium resources (2.09 wt% in the Earth's crust, 3.1 USD/kg vs Li 0.0017 wt%, 19.2 USD/kg) attract considerable research interests.[1-5] Nevertheless, most inorganic electrode materials in LIBs and Na-ion batteries (NIBs) do not extend their high performance to KIBs due to rigid crystalline structures and large volume changes caused by repeated insertion/de-insertion of K^+.[6-11] The ionic radius of K^+ (1.38 Å) is much larger than Na^+ (1.02 Å) and Li^+ (0.76 Å), resulting in large volume change, severe particle pulverization, and fast capacity decay in KIBs upon long-term cycling.[12-23] To achieve high-performance and sustainable KIBs, developing novel electrode materials with stable and flexible structures to accommodate the large volume change and enable fast reaction kinetics is critical.

As universal electrode materials, organic electrode materials (OEMs) with abundant structural diversity and high structural flexibility have been extensively studied in alkali-ion batteries, and have demonstrated exceptional performance of OEMs in LIBs, that can be retained in KIBs. However, state-of-the-art OEMs still suffer from three challenges: (1) low electronic conductivity, which leads to sluggish reaction kinetics; (2) particle pulverization due to large volume change during repeated K-ion insertion/de-insertion processes; and (3) high solubility in the electrolyte, which results in fast capacity decay.[3,24-29] To overcome these challenges and obtain

high-performance OEMs, the molecular structure design and organic electrode engineering is paramount. To reduce the solubility, salt formation is widely used because the formation of organic salts enhances the polarity and reduces the solubility of OEMs. To increase the conductivity and accommodate the large volume change, a highly conductive and large-surface-area host material such as graphene or porous carbon are used in organic electrodes to improve reaction kinetics, mitigate particle pulverization, and further decrease the dissolution of OEMs in the electrolyte.[30-32] Compared with inorganic anode materials,[33,34] the carboxylate-based anode materials have the advantages of low cost, abundance, high sustainability, and high structural tunability. Organic carboxylates are transition-metal-free and can achieve high theoretical capacity by rational structural design. Compared with organic anode materials,[35] the carboxylate-based anode materials have low redox potentials of < 1V, which make them ideal for developing high-performance anode for KIBs.

In this work, we presented a novel N-containing carboxylate salt as an anode material in KIBs. Scheme 1a shows the molecular structure of the N-containing carboxylate salt, $K_2C_{12}H_6N_2O_4$ (K-DCA), consisting of two pyridine moieties and two carboxylate groups in the *meta* position. The presence of these two pyridine moieties increases the available active sites in K-DCA and provides resonance stability during K-ion insertion/de-insertion, resulting in the reversible four-electron/K^+ redox mechanism (Scheme 1d). As shown in Scheme 1b, a carboxylate salt without pyridine moieties (Biphenyl-3,3'-dicarboxylic acid dipotassium salt, $K_2C_{14}H_8O_4$) was synthesized as a control. It is electrochemically inactive in KIBs and cannot reversibly react with K^+ and electrons (Scheme 1c), demonstrating the significant role of pyridine moieties in the electrochemical performance of the carboxylate anode. To optimize the electrochemical performance in KIBs, K-DCA was coupled with nitrogen-doped reduced graphene oxide (NrGO)

and a 2.8 M KPF_6-DEGDME electrolyte. The K-DCA-NrGO anode exhibits exceptional electrochemical performance. This work demonstrates a promising organic anode material for developing next-generation green and sustainable energy storage devices.

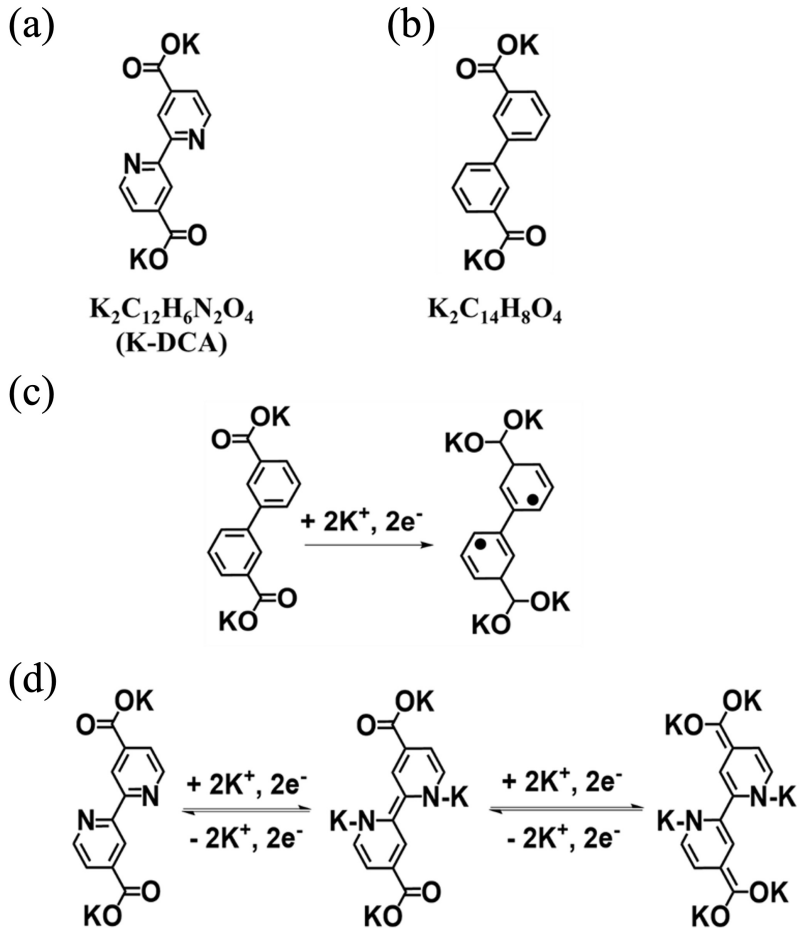

Scheme 1. The molecular structures of (a) $K_2C_{12}H_6N_2O_4$ (K-DCA) and (b) $K_2C_{14}H_8O_4$; (c) The proposed potassiation/de-potassiation mechanism of Biphenyl-3,3'-dicarboxylic acid dipotassium salt ($K_2C_{14}H_8O_4$); (d) The proposed potassiation/de-potassiation mechanism of $K_2C_{12}H_6N_2O_4$ (K-DCA).

2. Experimental procedure

2.1 Synthesis/Preparation of Electrode Materials

2,2'-bypyridine-4,4'-dicarboxylic acid dipotassium salt (K-DCA/$K_2C_{12}H_6N_2O_4$) was prepared as follows: 2,2'-bypyridine-4,4'-dicarboxylic acid (Alfa Aesar, 98%) was dispersed in ethanol with potassium hydroxide pellets (Sigma Aldrich, 85%) in 5% excess. The solution was stirred at room temperature for 24 hours, then the solution was filtered to collect the precipitate. The precipitate was washed with ethanol and dried in the vacuum oven at 90 °C overnight. The isolated product was a white powder.

2.2 Materials Characterization

The active material, 2,2'-bypyridine-4,4'-dicarboxylic acid dipotassium salt (K-DCA/$K_2C_{12}H_6N_2O_4$) was spectroscopically analyzed versus the starting material, 2,2'-bypyridine-4,4'-dicarboxylic acid as proof of synthesis; Fourier transform infrared spectroscopy (FTIR) was recorded by Agilent Cary 630 FTIR Spectrometer; Raman measurements were performed on a Horiba Jobin Yvon Labram Aramis using a 532 nm diode-pumped solid-state laser, attenuated to give ~900 μW power at the sample surface; Nuclear magnetic resonance (NMR) was recorded by Bruker Ascend 400; Powder X-ray diffraction (PXRD) pattern was recorded by Rigaku MiniFlex using CuKα radiation; and SEM images were taken by Hitachi SU-70 analytical ultra-high-resolution SEM (Japan) and Joel JSM-IT500HR/LV high-resolution SEM.

2.3 Fabrication of Electrodes and Assembly of Cells

The 2,2'-bypyridine-4,4'-dicarboxylic acid dipotassium salt (K-DCA/$K_2C_{12}H_6N_2O_4$) was mixed carbon black (CB) and polyvinylidene fluoride (PVDF) binder to form a slurry with the weight ratio of 60:30:10. The electrode was prepared by casting the slurry onto copper foil using a doctor

blade and dried in a vacuum oven at 90 °C overnight. The slurry coated on copper foil was punched into circular electrodes (K-DCA) with a mass loading of ~1.6 mg cm^{-2}. The mass loading of the active material in the K-DCA anode is ~0.96 mg cm^{-2}. Coin cells for K-ion batteries (KIBs) were assembled using potassium metal as the counter electrode, 2.8 M KPF_6 in diethylene glycol dimethyl ether (DEGDME) electrolyte, and glass fiber (Whatman) as the separator.

The 2,2'-bypyridine-4,4'-dicarboxylic acid dipotassium salt (K-DCA/ $K_2C_{12}H_6N_2O_4$) was mixed with nitrogen doped reduced graphene oxide (NrGO, ACS Material, LLC, Single layer graphene, N-doped Powder, 1g) in a 2:1 ratio and ball-milled for 10 minutes. This subsequent mixture was then mixed with carbon black (CB) and polyvinylidene fluoride (PVDF) binder to form a slurry with the weight ratio of 80:10:10. The electrode was prepared by casting the slurry onto copper foil using a doctor blade and dried in a vacuum oven at 90 °C overnight. The slurry coated on copper foil was punched into circular electrodes (K-DCA-NrGO) with a mass loading of ~1.6 mg cm^{-2}. The mass loading of the active material in the K-DCA-NrGO anode is ~0.85 mg cm^{-2}. Coin cells for K-ion batteries (KIBs) were assembled using potassium metal as the counter electrode, 2.8 M KPF_6 in diethylene glycol dimethyl ether (DEGDME) electrolyte, and glass fiber (Whatman) as the separator.

2.4 Electrochemical Measurements

All galvanostatic discharge-charge cycles were performed using an Arbin battery testing instrument (Arbin Instrument, model LBT20084) at room temperature in a voltage range of 0.4 – 2.0 V. The cells were first discharged then recharged. Specific capacity is calculated based on the mass of active material in the composite anode. Cyclic voltammograms (CVs) were recorded using Gamry Reference 1010E Potentiostat/Galvanostat/ZRA with a scan rate of 0.1 – 1.0 mV s^{-1}. Impedance analysis was also performed by Gamry Reference 1010E

Potentiostat/Galvanostat/ZRA. CVs at various scan rates were used to study the reaction kinetics of K-DCA and K-DCA-NrGO anode in KIBs. During the discharge/charge process, potassium ions insert into the anode and reversibly react with the two carboxylate groups at the *meta* position of the ring as well as the two nitrogens on the pyridine ring system, which is indicated in the potassiation/de-potassiation mechanism in Scheme 1d. Additionally, the K-DCA material consists of micro-sized particles (~1-5 μm) with aggregated nanorods clumped together, showing a high specific surface area. Hence, a partial capacitive behavior is exhibited due to monolayer adsorption of the ions at the electrode surface. In GITT test, the battery was discharged to 0.4V, and then charged back to 2V at the current density of 20 mA g^{-1}. During the cycling process, the battery was discharged or charged for 30 min, and then rest for 6h to reach the equilibrium potentials. To conduct the FTIR test before and after cycling, coin cells using K-DCA and K-DCA-NrGO, respectively, as the anode and potassium metal and the counter electrode were assembled. After cycling for 1, 10, and 20 cycles at 30 mA g^{-1}, the coin cells were disassembled in the glovebox. The cycled K-DCA and K-DCA-NrGO electrodes were washed using DEGDME and dried in a vacuum oven at 90 °C overnight. Then, the pristine and cycled electrodes were tested, and SEM images were taken by Joel JSM-IT500HR/LV high-resolution SEM. For the PXRD and FTIR tests before and after cycling, thick electrodes were prepared by using polytetrafluoroethylene (PTFE) as the binder. K-DCA was mixed with NrGO in a 2:1 ratio and ball-milled for 10 minutes. This subsequent mixture was then mixed with CB and PTFE binder in a ratio of 80:10:10. A thick film was obtained directly after grinding the mixture for 20 minutes. After drying in a vacuum oven at 90 °C overnight, the thick electrodes were assembled in coin cells and cycled for 1, 10, and 20 cycles at 30 mA g^{-1}. The coin cells were disassembled in a glovebox and the cycled electrodes

were washed using DEGDME and dried in a vacuum oven at 90 °C overnight. The pristine and cycled thick electrodes were tested by Rigaku MiniFlex and Agilent Cary 630, respectively.

3. Results and discussion

The structure of the nitrogen-containing potassium carboxylate, K-DCA, was confirmed and characterized by X-ray powder diffraction (PXRD), Fourier-transform infrared (FTIR) spectroscopy, proton nuclear magnetic resonance (^{1}H NMR), carbon-13 nuclear magnetic resonance (^{13}C NMR), and scanning electron microscopy (SEM). The PXRD pattern for K-DCA in Figure 1a (black) shows its crystalline structure, which is different from that of the precursor, DCA/$C_{12}H_8N_2O_4$, (Fig. S1a). FTIR for the carboxylate salt in Figure 1b (black) shows C=O asymmetric vibrational peaks at 1610 cm^{-1} and symmetric vibrational peaks at 1386 cm^{-1}. Compared with the FTIR spectrum of the precursor, DCA/$C_{12}H_8N_2O_4$, (Fig. S1b), the FTIR spectrum of K-DCA (Fig. 1b, black) shows the disappearance of the peaks at 2428 cm^{-1} (O-H vibrations) and 1707 cm^{-1} (C=O, asymmetric vibrations on the benzene ring), indicating the complete conversion of the dicarboxylic acid to the potassium carboxylate salt. New peaks can be observed at 1610 cm^{-1} and 1386 cm^{-1}, corresponding to the asymmetrical and symmetrical vibrations of C=O in the carboxylates, respectively, while the peak at 1546 cm^{-1} corresponds to the vibrations of C=N in the pyridine moieties of K-DCA. An enlarged and labeled spectra is presented in Figure S2a. The Raman spectroscopy was employed to further characterize NrGO, K-DCA, and the K-DCA-NrGO composite. In figure S2b, NrGO shows two sharp peaks for the disordered carbon (D band) and the graphitic carbon (G band) at 1351 cm^{-1} and 1591 cm^{-1}, respectively, while K-DCA exhibits the sharp peaks (Fig. S2c) at 1610 cm^{-1} and 1412 cm^{-1}, representing the asymmetric and symmetric stretching vibrations of C=O in the carboxylate group.

The sharp peak at 1554 cm^{-1} in figure S2c stand for the vibration of C=N in the pyridine moieties. The sloping baseline is ascribed to the fluorescence caused by the conjugated structure of K-DCA. In the spectrum for the K-DCA-NrGO composite (Fig. S2d), the two sharp peaks for the D band and G band of NrGO are still present, while the peak intensity of K-DCA is weakened because of the encapsulation by NrGO. The sloping baseline can still be observed due to the presence of K-DCA in the composite. The Raman results confirm the structure of K-DCA and the K-DCA-NrGO composite. Further characterizations for K-DCA using ^{1}H NMR (Fig. 1c) and ^{13}C NMR (Fig. 1d) with D_2O as the solvent were obtained. In Figure 1c, three ^{1}H NMR peaks in the range from 7.7 – 8.7 ppm represent the protons in the pyridine moieties of K-DCA, while no H signal from the unconverted dicarboxylic acid (at 13.846 ppm, Figure S1c), can be observed, demonstrating the successful formation of the potassium carboxylate. There is an obvious peak at 4.790 ppm, corresponding to the chemical shift of H in the D_2O solvent. The ^{13}C NMR spectrum of K-DCA (Fig. 1d) shows three peaks at 121.23 ppm, 123.23 ppm, and 149.61 ppm, corresponding to sp^2 carbons in the pyridine ring bonded with protons, while the peak at 146.30 ppm corresponding to sp^2 carbons in the pyridine ring bonded to the carboxylate groups. The ^{13}C NMR peak at 155.66 ppm, corresponding to sp^2 carbons in the pyridine rings bonded to each other, while the ^{13}C NMR peak at 173.00 ppm, corresponding to sp^2 carbons in the carboxylate groups. The surface morphology of the carboxylate was also investigated using SEM. In Figure 1e, it shows K-DCA consists of short rod-like particles with the size of 1~5 μm. These characterizations confirm the chemical structures and morphology of the N-containing carboxylate salt, K-DCA.

To investigate and confirm the effect of N in the ring system of K-DCA upon the electrochemical performance in KIBs, a conjugated carboxylate compound similar to K-DCA but without N, was also synthesized as an anode material. The structure of the conjugated potassium

carboxylate, $K_2C_{14}H_8O_4$, was confirmed and characterized by PXRD, FTIR, ^{1}H NMR, and ^{13}C NMR. The PXRD pattern in Figure S3a indicates the crystalline structure of $K_2C_{14}H_8O_4$. The FTIR spectrum (Fig. S3b) shows C=O asymmetric vibration peaks 1554 cm^{-1} and symmetric vibrational peaks at 1374 cm^{-1}. The ^{1}H NMR spectrum in Figure S3c shows four peaks in the range from 7.5~8.3 ppm (two peaks overlapping at 7.8 and 7.9 ppm), representing the protons in the biphenyl moieties of $K_2C_{14}H_8O_4$. There is an obvious peak at 4.8 ppm, corresponding to the chemical shift of H in the D_2O solvent. The ^{13}C NMR spectrum in Figure S2d shows four peaks at 127.26 ppm, 128.08 ppm, 129.06 ppm, and 137.02 ppm, corresponding to sp^2 carbons in the biphenyl ring bonded with protons, while the peak at 129.68 ppm corresponds to sp^2 carbons in the biphenyl ring bonded to the carboxylate groups. The ^{13}C NMR peak at 140.13 ppm corresponds to sp^2 carbons in the benzene rings bonded to each other, while the ^{13}C NMR peak at 175.36 ppm corresponds to sp^2 carbons in the carboxylate groups. The ^{1}H NMR and ^{13}C NMR spectrum further confirm the chemical structure of $K_2C_{14}H_8O_4$, which was employed as a control to compare with K-DCA in KIBs.

To optimize the electrochemical performance of K-DCA in KIBs, it was paired with nitrogen-doped reduced graphene oxide (NrGO). Addition of the highly conductive NrGO is used to facilitate the electron and ion transfer of the anode, accommodate large volume changes during repeated potassiation/de-potassiation processes, and form $\pi - \pi$ interactions with K-DCA, thereby increasing its stability during long-term cycling. The resulting composite, K-DCA-NrGO, was also characterized using PXRD, FTIR, and SEM. The PXRD pattern in Figure 1a (red) confirms the crystalline structure of K-DCA (black) is retained in the K-DCA-NrGO composite. The FTIR spectrum in Figure 1b (red) for the composite material, K-DCA-NrGO, further confirms the molecular structure of K-DCA is retained upon addition of NrGO since the asymmetrical and

symmetrical C=O vibrational peaks at 1610 cm^{-1} and 1386 cm^{-1} and C=N vibrational peak at 1546 cm^{-1} remain unchanged. The SEM image of K-DCA-NrGO (Fig. 1f) shows pulverized particles of K-DCA homogenously interspersed with NrGO sheets. These characterizations confirm the chemical structure and morphology of the composite, K-DCA-NrGO.

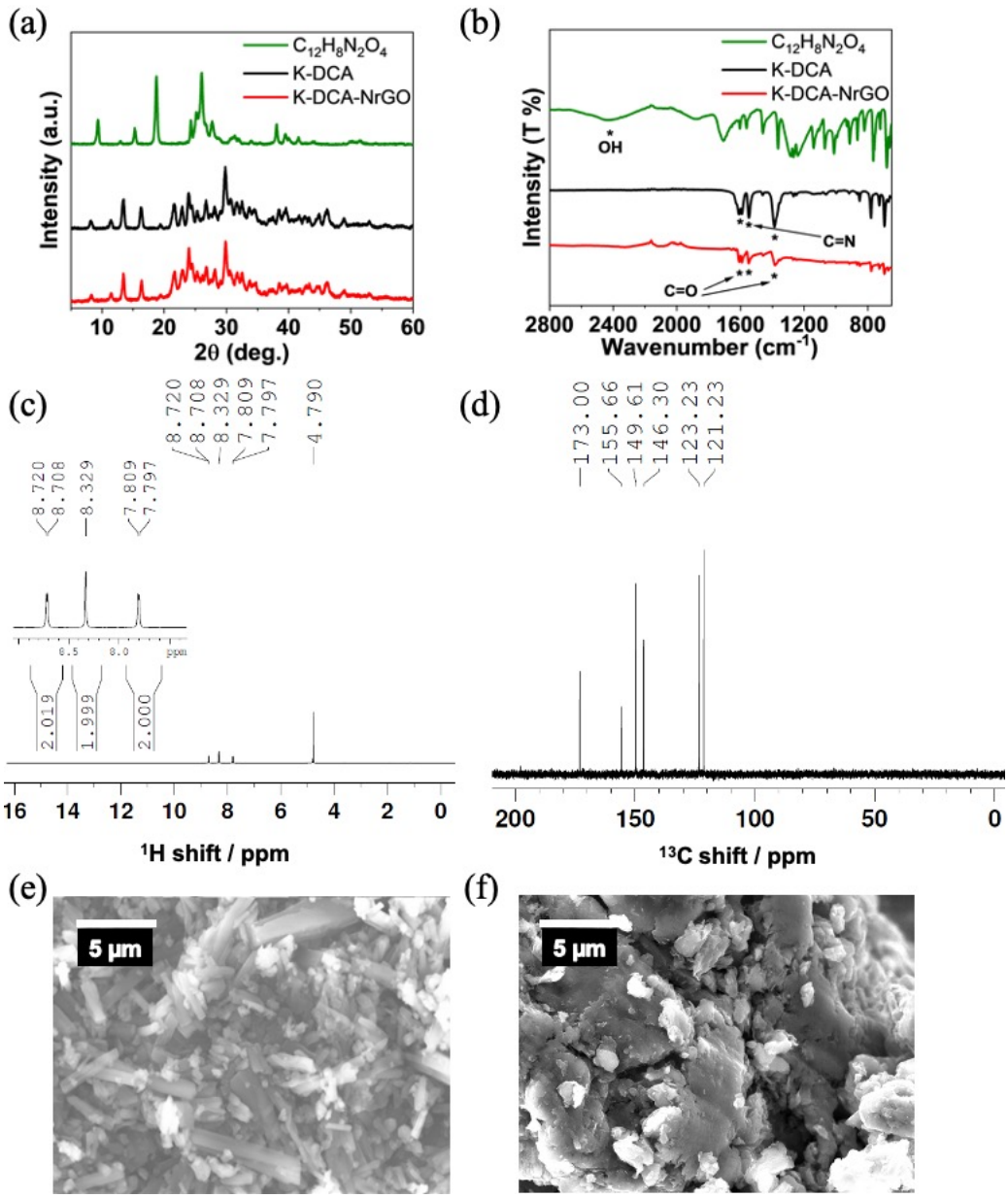

Fig. 1 Material characterizations of 2,2'-bypyridine-4,4'-dicarboxylic acid dipotassium salt (K-DCA) and 2,2'-bypyridine-4,4'-dicarboxylic acid dipotassium salt-NrGO (K-DCA-NrGO). (a)

PXRD pattern; (b) FTIR spectrum; (c) ^{1}H NMR spectrum with D_2O peak at 4.790 ppm; (d) ^{13}C NMR spectrum, and SEM images with scale bars of 5 μm of (e) K-DCA and (f) K-DCA-NrGO.

The electrochemical performance of the K-DCA anode was evaluated using potassium metal as the counter electrode and 2.8 M KPF_6 DEGDME as the electrolyte. Figure S4a shows the slopping charge/discharge curves with an average redox potential at ~0.8 V and a reversible capacity of 163.3 mAh g^{-1}. In the cyclic voltammetry (CV) result, a pair of cathodic peaks at ~0.5 V and ~0.9 V, as well as a pair of anodic peaks at ~0.45 V and ~0.8 V, are observed (Fig. S4b), corresponding to redox plateaus centered at ~0.8 V in Figure S4a. In the long-term cycling test (Fig. S4c), a reversible capacity of 88 mAh g^{-1} at 50 mA g^{-1} was achieved and retained after 100 cycles, demonstrating moderate cycling stability and diminished capacity retention. The K-DCA anode suffers from rapid capacity loss, and its capacity decreases to below 100 mA g^{-1} after 30 cycles. The Coulombic efficiency upon the long-term cycling was >99%. The contribution of carbon black to the reversible capacity of the K-DCA anode was subsequently measured and found to exhibit a reversible capacity of 60 mAh g^{-1} (Fig. S5). The rate capability of K-DCA (Fig. S4d) was measured from 20 mA g^{-1} – 2 A g^{-1}, and it demonstrated reversible capacities of 150.3 mAh g^{-1} and 40.6 mAh g^{-1}, respectively. After the current density reduces back to 20 mA g^{-1}, a reversible capacity of 103.2 mAh g^{-1} can be retained, demonstrating moderate reaction kinetics.

To fully investigate its performance and understand the effect of the pyridine moieties, a potassium carboxylate, $K_2C_{14}H_8O_4$, without the pyridine moieties was also exploited as the anode material. As shown in Figure S6a, the galvanostatic charge/discharge curves of $K_2C_{14}H_8O_4$ exhibit a pair of sloping plateaus centered at ~0.7 V with a specific capacity of only 23 mAh g^{-1} (Fig. S6b), which is contributed by the conductive carbon in the electrode. Hence, $K_2C_{14}H_8O_4$ is

electrochemically inactive as an anode in KIBs. The evaluation and comparison of $K_2C_{14}H_8O_4$ and K-DCA demonstrates that the pyridine moieties play a critical role in the electrochemical performance of K-DCA in KIBs, allowing for a reversible four-electron/K^+ redox mechanism to occur.

To enhance the performance of DCA in KIBs, the K-DCA-NrGO composite was used as the anode active material with potassium metal as the counter electrode and 2.8 M KPF_6 in diethylene glycol dimethyl ether (DEGDME) as the electrolyte. The galvanostatic charge/discharge curves of K-DCA-NrGO are shown in Figure 2a and exhibit one pair of redox plateaus centered at ~0.89 V with a reversible capacity of 225.3 mAh g^{-1}. The theoretical capacity of K-DCA is 335 mAh g^{-1} based on the four-electron reaction mechanism in Scheme 1d. The initial de-potassiation capacity of the K-DCA-NrGO anode achieved is lower than the theoretical capacity. This is ascribed to 1) the initial capacity loss triggered by the large volume change and organic material dissolution in the electrolyte; 2) the poor conductivity of the micro-sized K-DCA, which limits the material utilization; 3) the narrow cutoff window from 0.4V to 2.0V. Enlarging the cutoff window can increase the specific capacity at the price of worse cyclic stability. In the CV result, (Fig. 2b), a pair of cathodic peaks at ~0.7 V and ~1.1 V, and a pair of anodic peaks at ~0.8 V and ~1.1 V, are observed, corresponding to the redox plateaus centered ~0.89 V in Figure 2a. In long-term cycling test (Fig. 2c, Fig. S7), a reversible capacity of 115 mAh g^{-1} at 50 mA g^{-1} and 94 mAh g^{-1} at 200 mA g^{-1} were achieved and retained after 200 and 400 cycles, respectively, demonstrating excellent cycling stability and capacity retention. The Coulombic efficiency of the long-term cycling was >99%. However, the initial Coulombic efficiency of the K-DCA-NrGO anode is low. The reasons are 1) the initial Coulombic efficiency of carbon black and NrGO is low as shown in figure S5 and S8. This lowers the initial Coulombic efficiency of the K-DCA-NrGO

anode; 2) the anode was cycled in the cutoff window from 0.4V to 2.0V. The solid electrolyte interphase (SEI) will be generated in the initial cycles, which also lowers the initial Coulombic efficiency of the K-DCA-NrGO anode; 3) the anode suffers from obvious initial capacity loss due to the large volume change and dissolution of K-DCA as shown in figure 2c and 2d. This further lowers the initial Coulombic efficiency of the K-DCA-NrGO anode. The contribution of NrGO to the reversible capacity was subsequently measured and found to exhibit a reversible capacity of 71 mAh g^{-1} (Fig. S8). The capacity loss of organic carboxylate anodes is due to the dissolution of the active material in the electrolyte and large volume change caused by the repeated potassiation/de-potassiation process. To address these challenges, we used nitrogen-doped reduced graphene oxide and a concentrated electrolyte in this work. Other methods can also be used to improve the long-term cycling stability. For example, various types of carbon materials such as microporous or mesoporous carbon can be used to confine the carboxylate compounds, which not only mitigates the dissolution of the active material in the electrolyte but also accommodates the volume change upon cycling. In addition, the organic materials can be anchored to the carbon materials such as graphene or carbon nanotube by covalent bonds, which chemically stabilize the active material and alleviate the capacity loss. Moreover, different types of electrolytes such as fluorinated electrolytes or gel electrolytes can be employed to improve the long-term cycling stability of the organic anode materials. As shown in Figure 2e, rate capability of K-DCA-NrGO was measured from 20 mA g^{-1} – 2 A g^{-1} and demonstrated reversible capacities of 212.51 mAh g^{-1} and 72.98 mAh g^{-1}, respectively. After the current density reduces back to 20 mA g^{-1}, a reversible capacity of 133.38 mAh g^{-1} can be retained, demonstrating excellent reaction kinetics. Thus, confirming that the composite, K-DCA-NrGO is a promising organic anode for KIBs.

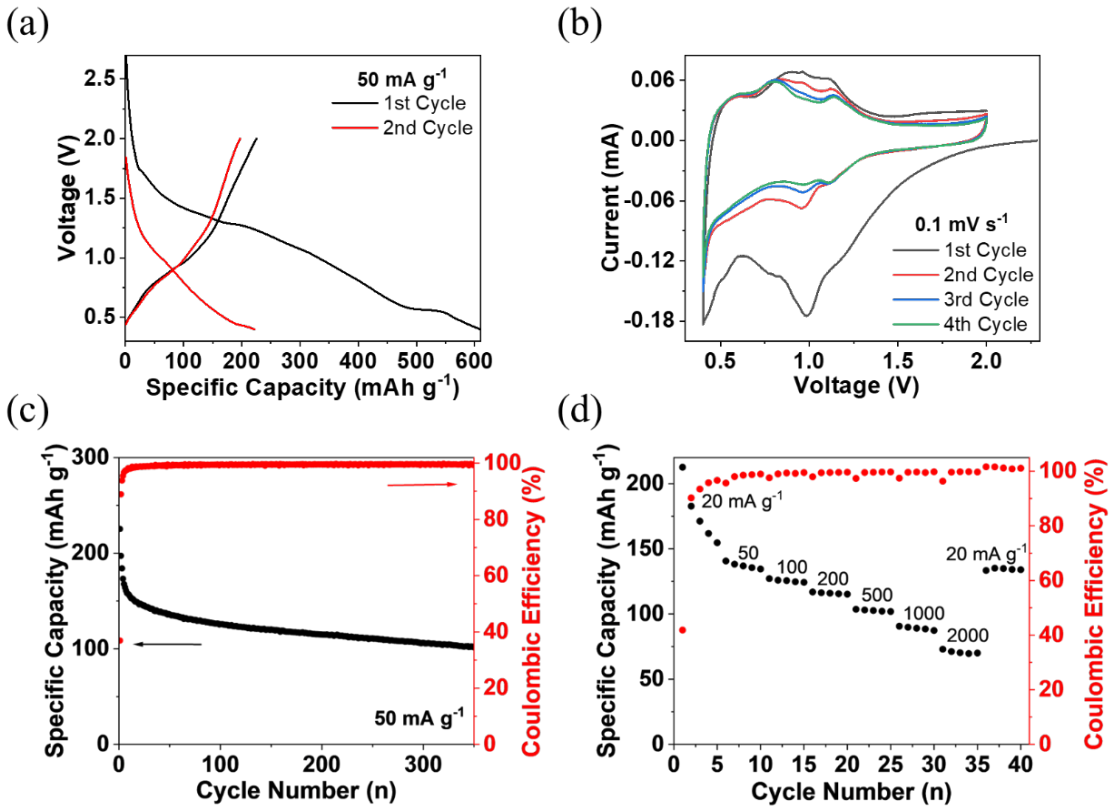

Fig. 2 Electrochemical performance of K-DCA-NrGO in KIBs. (a) Galvanostatic charge-discharge curves; (b) Cyclic voltammograms at 0.1 mV s^{-1}; (c) De-potassiation capacity and Coulombic efficiency versus cycle number at the current density of 50 mA g^{-1}; (d) Rate performance at various current densities.

To further explore the electrochemical properties and performance of K-DCA-NrGO in KIBs, CV, galvanostatic intermittent titration technique (GITT), and electrochemical impedance spectroscopy (EIS) were employed to study the reaction kinetics. In Figure 3a, the K-DCA-NrGO anode was cycled at various scan rates from 0.1 mV s^{-1} – 1 mV s^{-1}, the resulting voltammograms show that peak intensity increases with elevated scan rates. The linear fit of the natural logarithmic relationship of scan rate and the peak current was evaluated and is presented in Figure 3b and

shows cathodic and anodic slope (b) values of 0.7028 and 0.8196, respectively, indicating the reaction kinetics of K-DCA-NrGO exhibits a partial pseudo-capacitive behavior, which contribute to its fast reaction kinetics. The equilibrium potentials obtained from GITT are shown in Figure 3c and show the charge/discharge equilibrium potentials of K-DCA-NrGO are centered at 1.0/0.6 V with overpotentials of 44 mV and 42 mV at the charge and discharge plateaus, respectively. These small overpotentials further confirm the fast reaction kinetics of K-DCA-NrGO. Additionally, EIS was employed to evaluate the impedance evolution of the K-DCA-NrGO anode upon cycling. Presented in Figure 3d, the interfacial impedance of the fresh cell is ~18 ohms and slightly increases to ~28 ohms after 1 cycle. After 5, 10, and 20 cycles, the interfacial impedance was retained at ~34 ohms. The stable interfacial impedance from the 1st to 20th cycle demonstrates the stable SEI layer upon long-term cycling, which contributes to the stable cycle life. The CV, GITT, and EIS confirm fast reaction kinetics and the formation of a stable SEI layer of the K-DCA-NrGO anode in KIBs.

In comparison, the reaction kinetics of the pure anode material, K-DCA were also investigated by employing GITT and EIS. Presented in Figure S9a are the equilibrium potentials obtained from GITT, they show the charge/discharge potentials remain centered at 1.0 V/0.6V, respectively, however, the exhibited overpotentials (57 mV and 54 mV) are slightly larger than the overpotentials observed in the composite, K-DCA-NrGO, indicating that the addition of NrGO aides in improving the reaction kinetics of the anode material. EIS was additionally used to assess the impedance evolution of K-DCA upon cycling and is shown in Figure S9b, the interfacial impedance of the fresh cell is ~22 ohms and increases to ~71 ohms after 1 cycle. With continued cycling the interfacial impedance continues to increase from ~60 ohms after 5 cycles to ~67 ohms after 10 cycles, and ~76 ohms after 20 cycles. This indicates that the formation of the SEI layer in

the pure K-DCA anode is not optimal, resulting in its rapid capacity loss and diminished cycle life. These results confirm that NrGO plays a critical role in improving the reaction kinetics and cyclic stability of K-DCA.

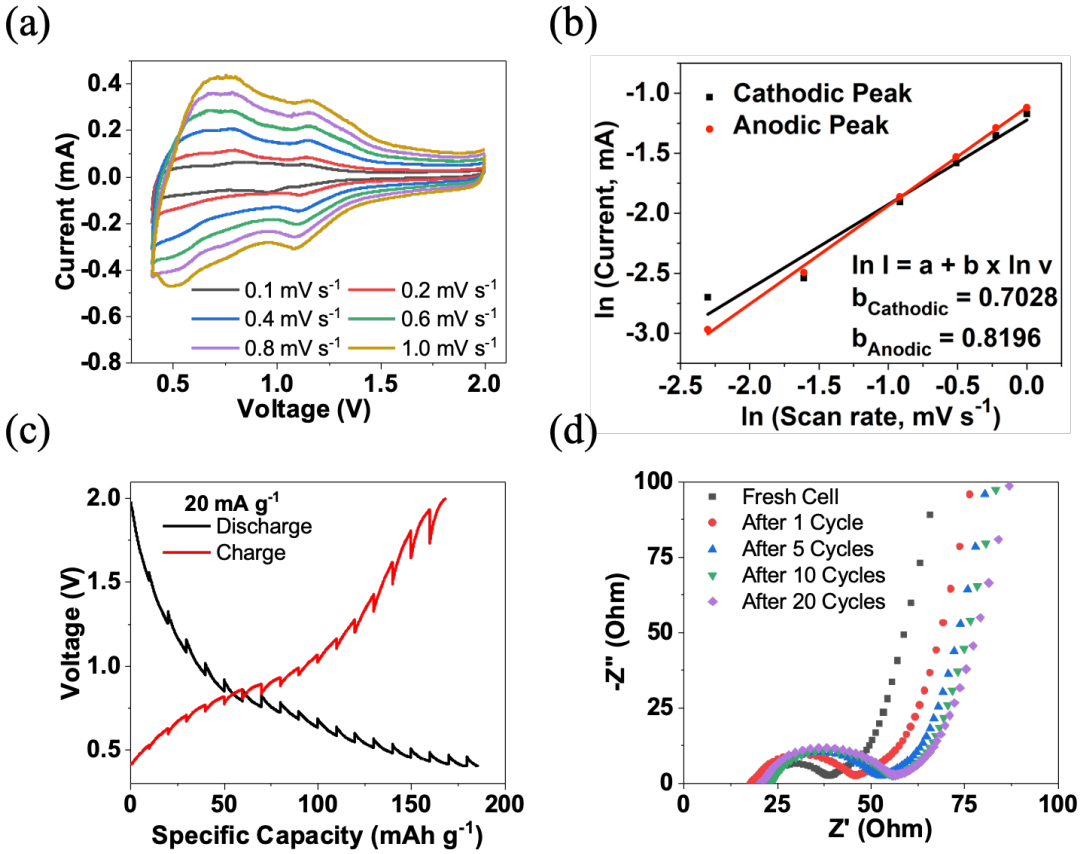

Fig. 3 Reaction kinetics of K-DCA-NrGO in KIBs. (a) Cyclic voltammograms at various scan rates; (b) The ln relationship of peak current and scan rate; (c) Potential response during GITT measurements at 20 mA g^{-1}; (d) Impedance analysis before and after charge/discharge.

Additionally, to investigate the crystalline, molecular, or morphological structural change of the K-DCA-NrGO anode upon cycling, PXRD, FTIR, Raman, and SEM were employed. In Figure 4a, the *ex-situ* PXRD patterns for the pristine and cycled anodes show that the crystalline

structure of K-DCA is changed after the first cycle, and the crystal structure becomes stable after the first cycle, indicating that the initial phase transformation is irreversible, and the newly formed crystalline structure is stable and reversible upon cycling. To examine any molecular structure changes resulting from cycling, FTIR was used. As shown in Figure 4b, the FTIR peaks for the pristine and cycled K-DCA-NrGO do not show visible changes before or after cycling, demonstrating that the molecular structure of the both K-DCA and NrGO are retained after potassiation/de-potassiation processes. Additionally, to explore and confirm the proposed redox mechanism, *ex-situ* Raman was employed to confirm the active sites in K-DCA during charge/discharge processes. Presented in Figure S10, the *ex-situ* Raman spectra shows that the Raman peaks for the carbonyl group and pyridine group in K-DCA disappear when fully discharged to 0.4 V. Upon charging to 2 V, the carbonyl and pyridine peaks re-appear, demonstrating a reversible electrochemical reaction between the K ions and both the carbonyl and pyridine groups. Finally, SEM imaging was used to gain insight into morphological changes of the pristine and cycled K-DCA-NrGO anodes. In Figure 4c-f, SEM images show small pores on the surface of the anodes (circled, measuring 3.626 μm) are created, as a result of large volume expansion, during repeated insertion/de-insertion of K ions during cycling. These morphology changes lead to the gradual capacity loss of the K-DCA-NrGO anode material during long-term cycling.

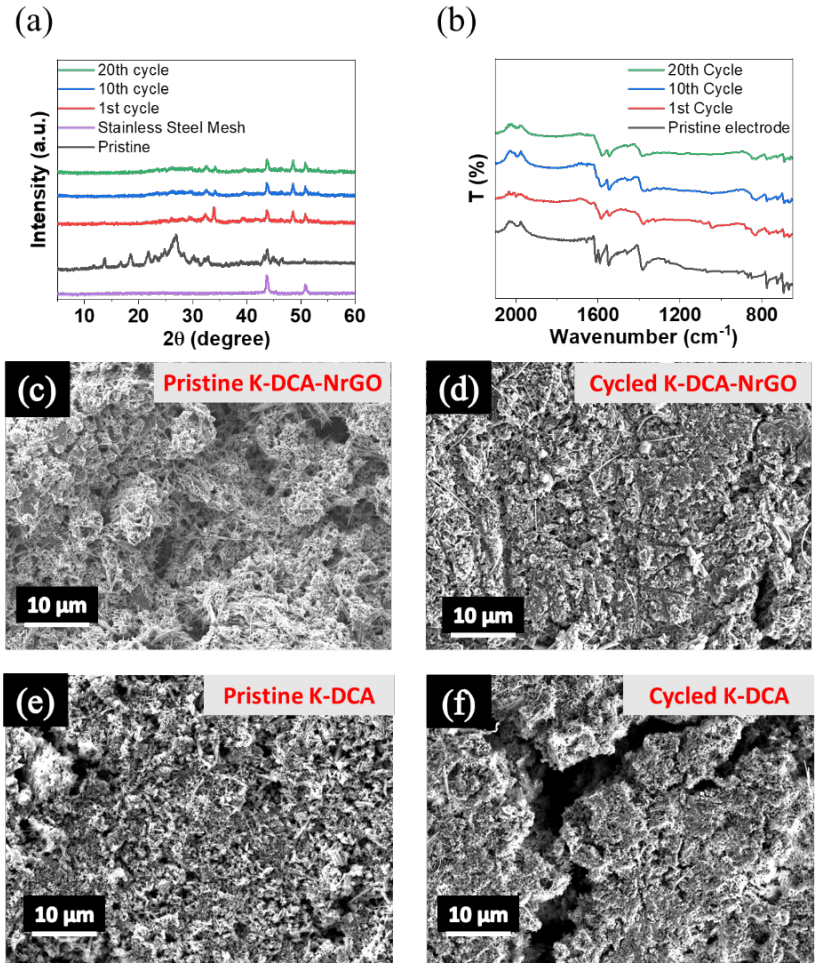

Fig. 4 Electrode characterizations before and after cycling. (a) ex-situ PXRD patterns of pristine and cycled K-DCA-NrGO anodes; (b) FTIR spectra of pristine and cycled K-DCA-NrGO anodes; SEM images of (c) pristine K-DCA-NrGO anodes, (d) K-DCA-NrGO anodes after 20 cycles, (e) pristine K-DCA anodes, and (f) K-DCA anodes after 20 cycles.

To compare with the K-DCA-NrGO anode, the pure K-DCA anode was also examined using FTIR and SEM to fully understand the stabilizing effects of NrGO upon cycled. In Figure S11, the FTIR of pristine and cycled K-DCA anodes does not show significant changes before or after cycling, demonstrating that the molecular structure of the pure anode material is stable. To

understand the morphological changes resulting from cycling, SEM was employed to examine the surface morphology of pristine and cycled K-DCA anodes and are presented in Figure 4e and 4f. These anodes show that large cracks, circled and measuring 5.409 μm (top) and 5.432 μm (bottom), are generated on the anode surface after 20 cycles. These obvious and extreme morphology changes are caused by repeated potassiation/de-potassiation processes which leads to the capacity loss observed during long-term cycling of K-DCA (Figure S4c). These results confirm that while the molecular structure of K-DCA is stable upon cycling, the morphology changes caused by the volume expansion/shrinkage during repeated potassiation/de-potassiation processes result in the significant capacity loss. Therefore, these results further confirm that the highly conductive NrGO is critical to improve the electrochemical performance of the organic anode, K-DCA, in KIBs.

To design redox-active carboxylate compounds, two or more carboxylate groups should be connected by a fully conjugated structure, consisting of strictly alternating carbon-carbon double and single bonds. However, when reacting with K ions, $K_2C_{14}H_8O_4$ will generate an instable radical intermediate rather than a stable product (Scheme 1b), so the reaction is irreversible, and $K_2C_{14}H_8O_4$ is electrochemically inactive. To activate the carboxylate groups in $K_2C_{14}H_8O_4$, the carbons on the *para* position of the benzene rings can be replaced by N to create extra active centers to alter the conjugation structure. For instance, K-DCA with N on the *para* positions contains four active centers, which are two carboxylate groups and two N in the pyridine moieties. The two N in the pyridine moieties firstly react with K^+ and electrons, and it triggers the rearrangement of the carbon-carbon double and single bonds (Scheme 1d), which reconnects the two carboxylate groups by a fully conjugated structure for further potassiation/de-potassiation reaction. All the active centers in K-DCA are connected by strictly alternating carbon-carbon

double and single bonds during the redox reaction, and K-DCA demonstrates a promising organic anode as evidenced in this work. Further structure design on the carbon in the *para* position of the benzene ring can be made. For example, other redox-active groups such as carboxylate, cyano, thiocarboxylate, etc. can be introduced to that position to create extra active centers and alter the conjugation structure for high-capacity and low-voltage organic carboxylate anodes in KIBs.

4. Conclusion

This work investigates a new N-containing carboxylate salt, K-DCA, with two carboxylate groups and two pyridine moieties. With the assistance of highly conductive and large-surface-area NrGO, the K-DCA-NrGO anode exhibits exceptional electrochemical performance in terms of high cyclic stability and robust reactions kinetics in KIBs. Our work proves that NrGO aids in enhancing electrode conductivity, decreasing active material dissolution through $\pi - \pi$ interactions with K-DCA, and accommodating large volume changes during repeated potassiation/de-potassiation processes. CV, GITT, and EIS analysis confirmed excellent reaction kinetics and the formation of a stable SEI layer, contributing to the good cycle life. While PXRD and FTIR analysis of pristine and cycled anodes further confirmed the formation of a stable crystalline structure after the first cycle and stable molecular structures upon cycling; and *ex-situ* Raman analysis confirmed the four-electron K^+ redox mechanism. This work proves the application and viability of K-DCA-NrGO as an anode material for sustainable K-ion batteries and opens opportunities for its continued investigation as a universal anode material in other battery systems.

Conflicts of interest

The authors declare no competing interests.

Acknowledgements

This work was supported by the US National Science Foundation (NSF) Award No. 2154145. The authors acknowledge the support from George Mason University Chemistry & Biochemistry Department and the George Mason University Quantum Science & Engineering Center.

References

1 C. P. Grey, and J. M. Tarascon, *Nat. Mater.,* 2016, **16**, 45–56.

2 J. Piątek, S. Afyon, T. M. Budnyak, S. Budnyk, M. H. Sipponen, and A. Slabon, *Adv. Energy Mater.,* 2021, **11**, 2003456.

3 K. Holguin, M. Mohammadiroudbari, K. Qin, and C. Luo, *J. Mater. Chem. A,* 2021, **9**, 19083-19115.

4 Y. Liang, C. Luo, F. Wang, S. Hou, S.-C. Liou, T. Qing, Q. Li, J. Zheng, C. Cui, and C. Wang, *Adv. Energy Mater.,* 2018, **9**, 1802986.

5 W. Zhang, W. Huang, and Q. Zhang, *Chem. Eur. J.,* 2021, **27**, 6131.

6 B. Wang, Y. Han, X. Wang, N. Bahlawane, H. Pan, M. Yan, and Y. Jiang, *IScience,* 2018, **3**, 110–133.

7 L. Xue, Y. Li, H. Gao, W. Zhou, X. Lü, W. Kaveevivitchai, A. Manthiram, and J. B. Goodenough, *J. Am. Chem. Soc.,* 2017, **139**, 2164–2167.

8 C. Zhang, Y. Xu, M. Zhou, L. Liang, H. Dong, M. Wu, Y. Yang, and Y. Lei, *Adv. Funct. Mater.,* 2017, **27**, 1604307.

9 Y.-H. Zhu, X. Yang, D. Bao, X.-F. Bie, T. Sun, S. Wang, Y.-S. Jiang, X.-B. Zhang, J.-M. Yan, and Q. Jiang, *Joule,* 2018, **2**, 736–746.

10 J. Liao, Q. Hu, X. He, J. Mu, J. Wang, and C. Chen, *J. Power Sources,* 2020, **451**, 227739.

11 Z. Zhang, M. Li, Y. Gao, Z. Wei, M. Zhang, C. Wang, Y. Zeng, B. Zou, G. Chen, and F. Du, *Adv. Funct. Mater.,* 2018, **28**, 1802684.

12 J. Han, G.-N. Li, F. Liu, M. Wang, Y. Zhang, L. Hu, C. Dai, and M. Xu, *Chem. Commun.,* 2017, **53**, 1805–1808.

13 J. H. Jo, J. U. Choi, Y. J. Park, Y. H. Jung, D. C. Ahn, T. Y. Jeon, H. S. Kim, J. Kim, and S. T. Myung, *Adv. Energy Mater.,* 2020, **10**, 1903605.

14 H. Kim, J. C. Kim, S. H. Bo, T. Shi, D.-H. Kwon, and G. Ceder, *Adv. Energy Mater.,* 2017, **7**, 1700098.

15 T. Masese, K. Yoshii, M. Kato, K. Kubota, Z. D. Huang, H. Senoh, and M. Shikano, *Chem. Commun.,* 2019, **55**, 985–988.

16 H. Zhang, K. Xi, K. Jiang, X. Zhang, Z. Liu, S. Guo, and H. Zhou, *Chem. Commun.,* 2019, **55**, 7910–7913.

17 X. Wu, D. P. Leonard, and X. Ji, *Chem. Mater.* 2017, **29**, 5031–5042.

18 Y. Liu, Y.-X. Lu, Y.-S. Xu, Q.-S. Meng, J.-C. Gao, Y.-G. Sun, Y.-S. Hu, B.-B. Chang, C.-T. Liu, and A.-M. Cao, *Adv. Mater.,* 2020, **32**, 2000505.

19 X. Q. Chang, X. L. Zhou, X. W. Ou, C.-S. Lee, J. Zhou, and Y. Tang, *Adv. Energy Mater.,* 2019, **9**, 1902672.

20 B. Ji, F. Zhang, N. Wu, and Y. Tang, *Adv. Energy Mater.,* 2017, **7**, 1700920.

21 H. B. Ding, J. Wang, L. Fan, Z. Liu, X. Jia, X. Yu, and B. Lu, *Chem. Eng. J.,* 2020, **395**, 125147.

22 H. Huang, J. Wang, X. Yang, R. Hu, J. Liu, L. Zhang, and M. Zhu, *Angew. Chem. Int. Ed.,* 2020, **59**, 14693.

23 M. Wang, W. Lu, H. Zhang, and X. Li, *Trans. Tianjin Univ.,* 2021, **27**, 1–23.

24 J. Heiska, M. Nisula, and M. Karppinen, *J. Mater. Chem. A,* 2019, **7**, 18735-18758.

25 S. Xu, Y. Chen, and C. Wang, *J. Mater. Chem. A,* 2020, **8**, 15547.

26 S. Muench, A. Wild, C. Friebe, B. Häupler, T. Janoschka, U. S. Schubert, *Chem. Rev.,* 2016, **116**, 9438–9484.

27 Z. Song and H. Zhou, *Energy Environ. Sci.,* 2013, **6**, 2280–2301.

28 C. Luo, Y. Zhu, Y. Xu, Y. Liu, T. Gao, J. Wang, and C. Wang, *J. Power Sources,* 2014, **250**, 372–378.

29 H. Wu, S. A. Shevlin, Q. Meng, W. Guo, Y. Meng, K. Lu, Z. Wei, and Z. Guo, *Adv. Mater.,* 2014, **26**, 3338–3343.

30 M. Lee, J. Hong, H. Kim, H.-D. Lim, S. B. Cho, K. Kang, and C. B. Park, *Adv. Mater.,* 2014, **26**, 2558–2565.

31 X. Fan, F. Wang, X. Ji, R. Wang, T. Gao, S. Hou, J. Chen, T. Deng, X. Li, L. Chen, C. Luo, L. Wang, and C. Wang, *Angew. Chem. Int. Ed.,* 2018, **57**, 7146–7150.

32 J. Hong, M. Lee, B. Lee, D.-H. Seo, C. B. Park, and K. Kang, *Nat. Commun.,* 2014, **5**, 5335.

33 B. John, V. Anoopkumar and T. D. Mercy, *ACS Appl. Energy Mater.*, 2020, **3**, 9478–9492.

34 C. H. Jo, J. H. Jo, J. U. Choi, H. Yashiro, H. Kim and S. T. Myung, *ACS Sustain. Chem. Eng.*, 2020, **8**, 3743–3750.

35 M. Zhang, W. Huang, Q. Huang, X. Yu, J. Wu, S. Di, H. Ye, Y. Wu and Y. Li, *Energy and Fuels*, 2021, **35**, 20367–20373.